Propofol Anesthesia Alters Cortical Traveling Waves

Propofol Anesthesia Alters Cortical Traveling Waves

Sayak Bhattacharya[1], Jacob A. Donoghue[1], Meredith Mahnke[1], Scott L. Brincat[1], Emery N. Brown[1,2,3], and Earl K. Miller[1]

Abstract

■ Oscillatory dynamics in cortex seem to organize into traveling waves that serve a variety of functions. Recent studies show that propofol, a widely used anesthetic, dramatically alters cortical oscillations by increasing slow-delta oscillatory power and coherence. It is not known how this affects traveling waves. We compared traveling waves across the cortex of non-human primates before, during, and after propofol-induced loss of consciousness (LOC). After LOC, traveling waves in the slow-delta (~1 Hz) range increased, grew more organized, and traveled in different directions relative to the awake state. Higher frequency (8–30 Hz) traveling waves, by contrast, decreased, lost structure, and switched to directions where the slow-delta waves were less frequent. The results suggest that LOC may be due, in part, to increases in the strength and direction of slow-delta traveling waves that, in turn, alter and disrupt traveling waves in the higher frequencies associated with cognition. ■

INTRODUCTION

Traveling waves are spatially organized patterns of activity whose peaks and troughs move sequentially across the brain. They have been observed in a variety of brain areas, including the cortex, and across a wide range of frequencies (from 1 to ~40 Hz; Muller, Chavane, Reynolds, & Sejnowski, 2018; Muller, Reynaud, Chavane, & Destexhe, 2014; Muller & Destexhe, 2012; Takahashi, Saleh, Penn, & Hatsopoulos, 2011; Ermentrout & Kleinfeld, 2001). Traveling waves were first observed under anesthesia in the visual cortex (Ebersole & Kaplan, 1981; Cowey, 1964) and later in the auditory (Reimer, Hubka, Engel, & Kral, 2011) and somatosensory cortices (Ferezou, Bolea, & Petersen, 2006). Their prominence under anesthesia (Liang et al., 2021; Townsend & Gong, 2018; Sato, Nauhaus, & Carandini, 2012; Nauhaus, Busse, Carandini, & Ringach, 2009; Benucci, Frazor, & Carandini, 2007) may be because of lower background noise (Muller et al, 2018). Traveling waves are also evident in cortex during sleep (Muller et al., 2016; Massimini, Huber, Ferrarelli, Hill, & Tononi, 2004) and early development (Watt et al., 2009; Wong, Meister, & Shatz, 1993). However, they are also present in the awake adult cortex (Sreekumar, Wittig, Chapeton, Inati, & Zaghloul, 2020; Alamia & VanRullen, 2019; Takahashi et al., 2011; Prechtl, Cohen, Pesaran, Mitra, & Kleinfeld, 1997) and hippocampus (Zhang, Watrous, Patel, & Jacobs, 2018; Lubenov & Siapas, 2009). In fact, there is a growing realization that traveling waves show properties that have functional advantages. They can be planar or rotational (Bhattacharya, Brincat, Lundqvist, & Miller, 2022; Muller et al., 2016; Ermentrout & Kleinfeld, 2001). They tend to flow in certain (not random) directions, vary in different degrees of organization and scale (Muller et al., 2018). They travel in speeds that are correlated with their frequency (Bhattacharya et al., 2022; Zhang & Jacobs, 2015). Faster waves are purported to travel further than slower waves (Bhattacharya & Iglesias, 2019). In other words, traveling waves can have precise properties that, in turn, can induce timing relationships into networks.

This can (and seems to) serve a variety of cortical functions. Traveling waves can foster memory consolidation. During sleep spindles, rotating waves reliably repeat the precise timing offsets needed for spike-time-dependent plasticity (Muller et al., 2016). Traveling waves may help "read out" information. A correlation between traveling wave phase and reaction time suggests their role in memory retrieval (Mohan, Zhang, & Jacobs, 2022). Waves travel in different directions depending on whether sensory processing or memory retrieval is being performed (Mohan et al., 2022; Alamia & VanRullen, 2019). Traveling waves also seem to play a role in perception. The timing and position of traveling waves in visual cortex regulates spiking to, and the animal's ability to detect, visual targets (Davis, Muller, Martinez-Trujillo, Sejnowski, & Reynolds, 2020). Finally, traveling waves may also serve fundamental network functions like retaining recent history of network activations, keeping track of time, and they may even perform computation (Heitmann & Ermentrout, 2020; Muller et al., 2018; Muller & Destexhe, 2012; Ermentrout & Kleinfeld, 2001).

Although traveling waves have been studied in both anesthetized and awake animals, they have not been

[1]The Picower Institute for Learning and Memory and Department of Brain and Cognitive Sciences, Massachusetts Institute of Technology, Cambridge, MA, [2]The Department of Anesthesia, Critical Care and Pain Medicine, Massachusetts General Hospital/Harvard Medical School, Boston, MA, [3]The Institute for Medical Engineering and Science, Massachusetts Institute of Technology, Cambridge, MA

Journal of Cognitive Neuroscience 34:7, pp. 1274–1286
https://doi.org/10.1162/jocn_a_01856

directly compared between anesthetized and awake states. This is relevant because of their potential roles in cortical function and, hence, normal consciousness. However, it is particularly relevant because of recent studies showing that propofol, a widely used anesthetic, profoundly affects oscillatory dynamics in cortex (Bastos et al., 2021; Redinbaugh et al., 2020; Purdon, Sampson, Pavone, & Brown, 2015; Purdon et al., 2013; Lewis et al., 2012). Following loss of consciousness (LOC), the cortex of nonhuman primates (NHPs) showed strong increases in low-frequency slow-delta (~1 Hz) local field potential (LFP) power and coherence. This reversed when propofol was ceased and the NHPs regained consciousness. In other words, propofol does not merely "turn off" cortex. It profoundly changes cortical rhythms. It is thus likely to affect traveling waves as well.

Thus, we re-examined data from our previous study of the effects of propofol on cortical oscillatory power and coherence (Bastos et al., 2021). We used methods recently employed to identify and document traveling wave properties in cortex (Bhattacharya et al., 2022). Recordings were made from electrode arrays in three cortical areas: the ventrolateral prefrontal cortex (vlPFC), FEFs, and the auditory parabelt cortex of macaque monkeys. The NHPs transitioned from awake to LOC upon propofol administration, and then back to awake state upon propofol cessation. Propofol-induced LOC increased slow-delta traveling waves, strengthened their organization, and caused them to travel in different directions relative to the awake state. There was a corresponding decrease in higher-frequency (8–30 Hz) traveling waves. In fact, the slow-delta traveling waves seemed to "crowd out" high-frequency traveling waves, causing them to flow in directions where the slow-delta waves were less frequent.

METHODS

Subjects, LFP Recordings, and Propofol Administration

Experimental data were used from our earlier article (Bastos et al., 2021). Two rhesus macaques (*Macaca mulatta*) aged 14 years (Subject 1, male, ~13.0 kg), and 8 years (Subject 2, female, ~6.6 kg) participated in these experiments. Detailed surgical and housing protocols can be found in the work of Bastos et al. (2021).

Experimental sessions were carried out in two phases. In the first phase, a period of 15–90 min of awake baseline activity was recorded. Next, propofol was intravenously infused via a computer-controlled syringe pump (PHD ULTRA 4400, Harvard Apparatus). The infusion protocol was stepped such that unconsciousness was induced via a higher rate infusion (285 μg/kg/min for Subject 1; 580 μg/kg/min for Subject 2) for 20 min before dropping to a maintenance dose (142.5 μg/kg/min for Subject 1; 320 μg/kg/min for Subject 2) for an additional 40 min.

Facial movements and pupil size were tracked by infrared (Eyelink 1000 Plus, SR-Research) throughout the sessions. The instant of eyes-closing that persisted for the remainder of the infusion was marked as LOC. Recovery of consciousness (ROC) was marked by the instant of the first to occur between eyes reopening or regaining of motor activity following propofol infusion cessation. Further details can be found in the work of Bastos et al. (2021). All procedures followed the guidelines of the MIT Animal Care and Use Committee (protocol number 0619-035-22) and the US National Institutes of Health.

The subjects were chronically implanted with 8 × 8 iridium-oxide Utah microelectrode arrays (1.0 mm length, 400 μm spacing; Blackrock Microsystems) in the vlPFC, FEFs, and the auditory parabelt cortex (caudal parabelt). Signals were recorded on a Blackrock Cerebus. LFPs were recorded at 30 kHz and filtered on-line via a low-pass 250-Hz software filter and downsampled to 1 kHz. All preprocessing and analysis were performed in Python or MATLAB (The MathWorks, Inc). Quality control during recording assured that any electrodes with poor impedance or a lack of signal were marked as missing. For the power analysis, the resulting signals were convolved with a set of complex Morlet wavelets.

LFP Spatial Phase Maps

The raw LFP traces were filtered in the desired frequency range, using a fourth-order Butterworth filter for alpha (8–12 Hz) and beta (12–30 Hz) ranges, and a third-order Butterworth filter for slow-delta (0.5–3 Hz) oscillations, forward-reverse in time to prevent phase distortion (see MATLAB function *filtfilt*). A Hilbert transform was used to obtain the analytical signal for each electrode. The phase of each electrode for the 8 × 8 array is called the "phase map" for that time instant. These phase maps (unsmoothed) were checked for gradients to identify traveling waves.

Shuffling Procedure

To ensure that the probability of detecting traveling waves exceeded that expected by chance, we performed a random shuffling procedure to establish a threshold for the correlation coefficient—beyond which a traveling wave was counted. This was done by shuffling the phase values on the array randomly (with 25 different types of random permutations) and calculating the correlation coefficient. The 99th percentile of the resulting distribution of coefficient values determined a threshold (0.3) above which the correlation exceeded chance.

Traveling Wave Identification and Classification

We used circular statistics to identify wave patterns. Methods followed our previous investigation of traveling waves in the prefrontal cortex (Bhattacharya et al., 2022).

The circular–circular correlation coefficient reports the spatial gradient similarity between two phase maps that are adjusted to account for circular phase values. For the

signal phase (φ at each array coordinate $[a, b]$) and the rotation angle (θ) around the chosen point, the circular–circular correlation coefficient thus was as follows:

$$\rho_c = \frac{\Sigma_{ab} \sin(\varphi_{ab} - \varphi_m) \sin(\theta_{ab} - \theta_m)}{\sqrt{\Sigma_{ab} \sin^2(\varphi_{ab} - \varphi_m) \sin^2(\theta_{ab} - \theta_m)}}$$

$$\theta_m = \mathrm{Arg}\left(\sum_{ab} e^{i\theta_{ab}}\right)$$

As we showed in our previous study (Bhattacharya et al., 2022), the choice of point around which the coefficient was calculated split the array into two regions (Figure 1E). A traveling wave toward the positive half (red arrows, Figure 1E) would result in positive values, whereas the opposite direction would result in negative values. Each chosen point had a "chance zone" around which the coefficient values would be too low (less than the threshold determined by the shuffling permutation procedure) to make a conclusion regarding wave existence. Hence, two points, (1, 4̄) and (4̄, 1), chosen such that their chance zones did not overlap, were used to determine wave existence (Figure 1E). If either point reported a coefficient value greater than the permutation threshold, a wave was counted. Furthermore, a combination of the two coefficient values could thus be used to bin the waves into four directions (Figure 7A): $\rho_{c14} > 0$, $\rho_{c41} > 0$ (red direction), $\rho_{c14} > 0$, $\rho_{c41} < 0$ (green direction), $\rho_{c14} < 0$, $\rho_{c41} > 0$ (blue direction), and $\rho_{c14} < 0$, $\rho_{c41} < 0$ (black direction). As this was an 8 × 8 array (even numbers), it is understandable that the bisecting axis was not perfectly horizontal for ρ_{c14} or perfectly vertical for ρ_{c41}. In addition, it is important to note that our methods were not dependent upon the exact choice of points (Bhattacharya et al., 2022).

Using this algorithm, we identified time instants where traveling waves existed. This did not differentiate between short-lived waves and continuous wave cycles. This also ensured that we identified continuous phase gradients on the array and not just phase-jumps (corresponding to a pulse).

To distinguish between planar and rotating waves, similar to our earlier study (Bhattacharya et al., 2022), we used a third rotation map around (4, 4̄) along with the (1, 4̄) and (4̄, 1) maps. Each wave instant thus had its associated three coefficient values: ρ_{c14}, ρ_{c41}, and ρ_{c44}. Using simulations, we obtained similar coefficient values for different types of planar and rotating waves. Waves were simulated using the following equations (Muller et al., 2016):

$$g(t, \varphi) = Ae^{i(wt - k\varphi)} + \sigma\gamma(t)$$

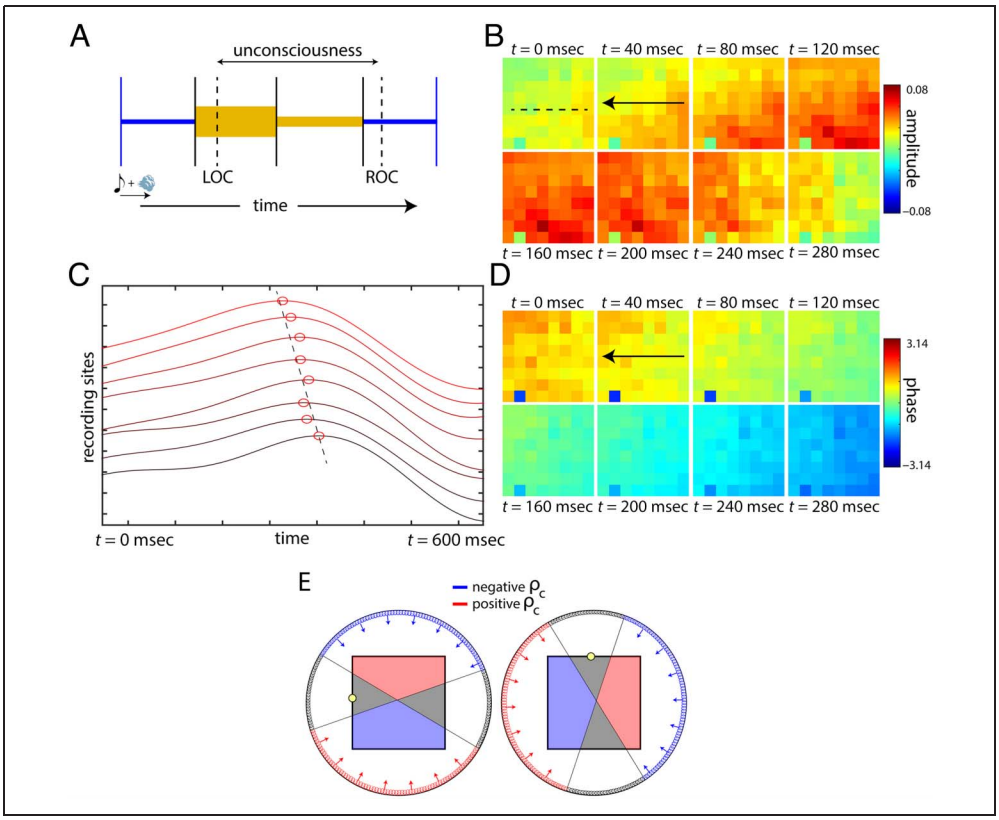

Figure 1. (A) The experimental setup, consisting of periodic sensory stimulation using a tone followed by an airpuff. Propofol (yellow) administered in two phases. The first phase was a higher dose to induce LOC, followed by a lower dose for LOC maintenance. After propofol cessation ROC occurred. (B) LFP amplitudes (slow-delta) observed across the 8 × 8 recording array during the awake state of Animal 2. Arrow indicates direction of wave propagation. (C) Voltage traces from one row of the array (dashed line in B), with peaks marked. Dashed line indicates sequential shifts in peak. (D) Phase maps corresponding to amplitude maps in (B). (E) Wave quantification method based on choice point (yellow). Red region (red arrows) indicates positive coefficient waves, whereas blue denotes negative. Gray region denotes areas for which wave existence could not be conclusively concluded for that choice point, that is, the coefficient value was less than the shuffling permutation threshold (see Methods section).

where φ was the input phase map, w was the temporal frequency, and k was the spatial wavenumber (1/wavelength). The second term was a Gaussian white noise term, with zero mean and standard deviation σ.

In this way, we obtained the three coefficient values for simulated waves, to go with our experimental coefficient data set. We compared these values to automatically classify the type of wave observed, based on the Euclidean distance between a wave type and the observed phase map. Coefficient matching with three different maps allowed for greater accuracy with lesser chances of misclassification. It is important to note that owing to the size and placement of the recording array, it was possible, if not likely, that only a part of the rotating waves was being captured on the array. Our algorithms were able to capture these "wavelets."

Wave speed at a time instant was calculated from the phases (p) by dividing the temporal frequency ($\partial p/\partial t$) at that time with the spatial frequency ($\partial p/\partial x$; Zhang & Jacobs, 2015). The gradients obtained were averaged across electrodes to get the net wave speed for that time instant.

Wave Spatial Coherence

The amplitude envelope obtained from the Hilbert transform of the LFP signal was used to determine the spatial coherence of the traveling wave. A wave was deemed to be spatially coherent when it showed similar amplitudes across the array at a particular instant. A broken wave would show a larger amplitude variance across electrodes on the same array. We demonstrated this using two simulations: (1) where the array elements had uniform oscillation amplitude ranges, and (2) where the amplitude ranges were randomly distributed (analogous to a fragmented cortex). When the same phase gradient (traveling wave, left to right; Figure 3A) was imposed in both cases, the first showed a smooth, organized wave structure (Figure 3A, top), whereas the other showed a broken traveling wave with heterogeneous amplitudes across the wave band. For the broken wave, the amplitude envelope showed larger variance when compared with the more solid wave. The coefficient of variation was defined as the standard deviation divided by the mean.

Wave Similarity Analysis

Two phase maps were checked for similarity by computing the circular–circular correlation between them (Muller et al., 2016). A high positive coefficient value indicated similar waves, that is, waves with the same phase organization on the array. A high negative coefficient value indicated antisimilar mirror-image type waves. A coefficient around zero (shaded region, Figure 6, with the threshold determined by the shuffling permutation procedure) indicated no conclusive similarity between the phase maps. This analysis was done across all time instants in each session.

Statistical Tests

All of our statistical tests were based on the one-sample t test (two-tailed), between two groups of data where each group composed of 20 data points (corresponding to the number of experimental sessions). We report if the changes observed in a particular time period are significantly different ($p < .01$) from the awake baseline average (marked on the plot). If the difference for the time period is significantly different, a dot (colored corresponding to the frequency range being assessed) was added below that time period. No cross-frequency comparison was done. The goodness of fit for the similarity data in Figure 6 was measured by calculating the root means square error for a curve-fitting between the data shown and a sum of two Gaussian functions with opposite signed means (0.5 and −0.5). The root means square error values for the fit were as follows:

Slow-delta waves: 0.027 (baseline), 0.009 (post-LOC) – error reduced threefold.

Alpha waves: 0.028 (baseline), 0.024 (post-LOC).

Beta waves: 0.026 (baseline), 0.024 (post-LOC).

RESULTS

Here, we re-examined data from our study of the neural effects of propofol (Bastos et al., 2021). Two macaque monkeys were used. Throughout each experimental session, they were exposed to sensory stimulation. A tone was presented every 5–7 sec followed by, after a 0.5 sec gap, a puff of air that was blown toward the eyes (Figure 1A). This was used to test their responsiveness to external stimulation (the airpuff). It, along with other metrics (see below), was used to assess state of consciousness.

Propofol was administered (see Methods section) in two phases (Figure 1A). First, a higher dose (280–580 μg/kg/min) of propofol was administered to induce LOC. LOC was deemed at the timestamp where the subject's eyes closed and did not reopen for the remainder of the infusion. Soon afterward, the propofol infusion rate was reduced to a lower level (140–320 μg/kg/min) that could still maintain LOC. Later, propofol infusion was ceased. After a brief period, there was ROC.

We used the same markers for LOC and ROC as our previous study (for details and analysis, see the work of Bastos et al., 2021; Figure 1). They included behavioral responsiveness to the air puff, heart-rate, blood oxygenation levels, EMG variance and tone, and so forth. Sensory stimulation was held constant throughout the entire experimental session to ensure that the awake and unconscious states were identical, other than the anesthesia.

LFPs were recorded from a total of 6 Utah arrays, three in each animal, placed in the vlPFC, the FEFs, and the caudal parabelt. Each array consisted of 64 electrodes (8 × 8 pattern) with a 400-micron spacing (for exact placement and other details, see the work of Bastos et al., 2021). We analyzed LFPs for spatiotemporal

signatures of traveling waves, using the same analytical methods as Bhattacharya et al. (2022).

Detecting and Quantifying Traveling Waves

A traveling wave is a sequential activation of adjoining neural groups that gives the appearance of a traveling front of activity. An example is shown in Figure 1B for an array in the vlPFC. It plots LFP amplitudes band-pass filtered to show the slow-delta band (0.5–3 Hz) only. This was recorded during a "baseline" interval before administration of propofol, while the animal was awake. Each tile represents an electrode. Red (blue) indicates higher (lower) LFP amplitudes. Across time, higher amplitudes move sequentially across the array. For example, the first panel (0 msec) shows a high-amplitude peak near the right of the array. With each time step, the peak amplitudes "move" toward and through the middle of the array and then toward the left.

Traveling waves could be detected by observing the gradient in oscillation phase values across the recording array (Bhattacharya et al., 2022). Figure 1C shows oscillatory phases (demodulated using the Hilbert transform) across time on one row of the array (dashed black line in first panel of Figure 1B). The sequential shift in phase across adjacent electrodes and time is indicative of a traveling wave. The phase plots for the whole array are shown in Figure 1D. Note the progressive increase in phase from the right to the left. The wave was not just a "pulse" (a single front or edge of activity moving across the array). A phase gradient could be seen in front of and behind the peak amplitudes, indicating a traveling wave rather than a traveling "pulse."

We quantified traveling waves using circular–circular correlation coefficients to measure the phase gradient (adjusted for circularity in phase values, see Methods section). The coefficient value (ρ_c) indicates the spatial correlation between the observed phase map at a given time instant and an idealized rotational phase map around a particular "choice point" on the array. If this correlation was greater than a threshold (determined through a shuffling permutation process; see Methods section), a wave was counted for that time instant. A positive versus negative ρ_c indicates wave movement in two opposite directions across the electrode array (Figure 1E).

To accurately assess wave movement, however, we needed two choice points. This is because the classification of wave directions depended on the choice point. For example, consider the array shown in Figure 1E. Two different choice points on the array are shown in Figure 1E, left and right. With one choice point (circle, Figure 1E, left), waves directed toward the red region in Figure 1E (left) showed positive correlation ($\rho_c > 0$) whereas the blue waves showed negative correlation. With a different choice point (Figure 1E, right), the waves also binned into positive and negative directions but the directions that corresponded to positive versus negative were different. In both cases, some of the waves for one choice point would be directed toward the gray zone (i.e., below threshold for classification as a wave) for the other choice point. Thus, to accurately classify all waves, we needed two points that binned waves in orthogonal directions. This captured all waves with none erroneously falling into the gray zone. If the coefficient for either choice point showed a value greater than the threshold value, a wave was counted. This rendered results independent of any one choice point (Bhattacharya et al., 2022).

Changes in the Number and Speed of Traveling Waves after Propofol-induced LOC

We observed traveling waves in three frequency bands (slow-delta = 0.5–3 Hz, alpha = 8–12 Hz, and beta = 12–30 Hz). After propofol-induced LOC, there were changes in the number of traveling waves. Figure 2A shows

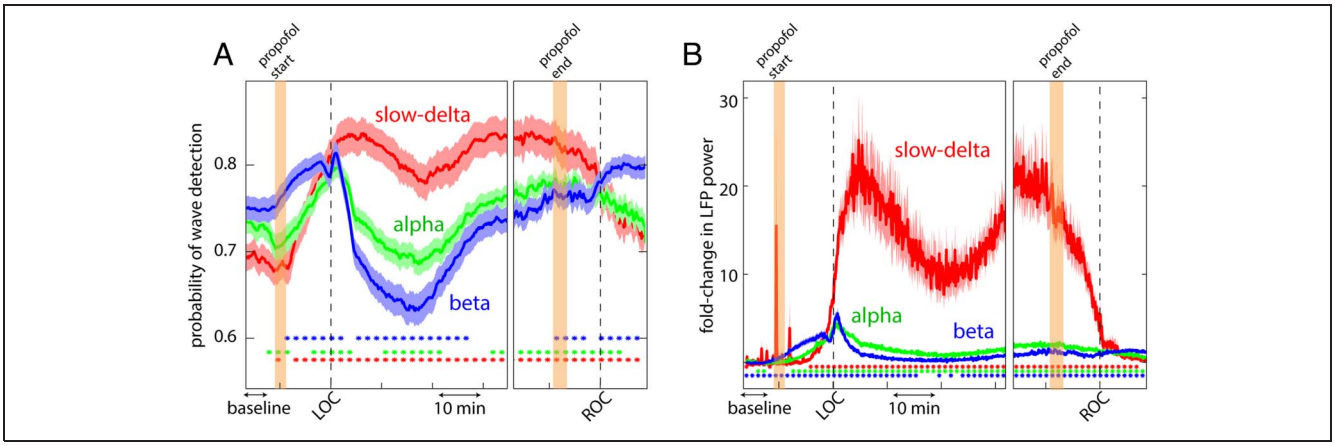

Figure 2. (A) Probability of wave detection in three frequency ranges across time, averaged across sessions and arrays. The dots denote statistical significance from baseline (marked). (B) Fold change in LFP power compared with baseline (marked) across time, averaged across sessions and arrays. The dots denote statistical significance compared with baseline (t test, $p < .01$).

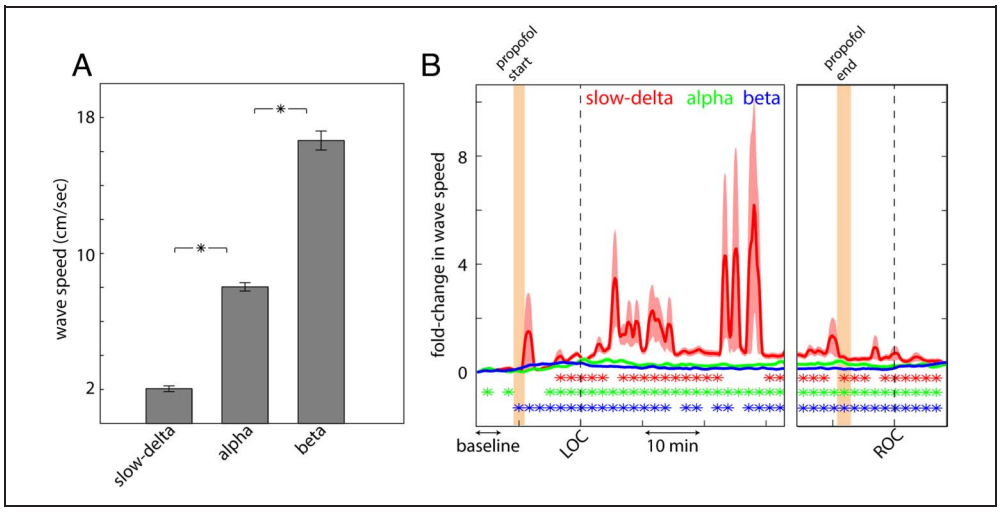

Figure 3. (A) Wave speeds observed in the three frequency ranges, averaged across all time (irrespective of propofol), sessions, and arrays. An asterisk denotes statistically significant differences from baseline for each frequency band (*t* test, $p < .01$). (B) Fold change in wave speeds compared with baseline (marked) across time, averaged across sessions and arrays. The colored asterisks denote statistical significance (blue for beta, green for alpha, and red for slow-delta compared with baseline) from baseline.

the wave counts in each of three frequency bands, averaged across sessions and arrays, from the awake state through LOC and then from LOC through ROC. Wave counts in all bands increased shortly after propofol infusion began (before LOC, orange-shaded area). The number of alpha (in green) and beta (in blue) waves peaked around the time of LOC. Slow-delta waves (in red) peaked shortly after LOC. Throughout LOC, slow-delta waves showed a large and significant increase in wave counts relative to the baseline period before infusion of propofol (Figure 2A, baseline marked). There was a good degree of variance in slow-delta wave speeds across the population. By contrast, beta waves decreased after LOC, relative to baseline. Alpha waves (8–12 Hz) showed an intermediate response, that is, were more similar to the prepropofol baseline state than slow-delta and beta. After propofol administration ceased (shown in orange, Figure 2A, right), the wave counts started to move toward prepropofol baseline values.

Plots of LFP power (independent of waves; Figure 2B) showed correspondingly large increases in slow-delta oscillations after LOC relative to alpha and beta. This converged back to baseline levels after propofol cessation. Spectrograms showing details of these power changes can be found in the work of Bastos et al. (2021).

Propofol also increased traveling wave speed, especially in the slow-delta band. Oscillation frequency and wave speeds, as expected, were positively correlated (Zhang & Jacobs, 2015). They were around the 1- to 20-cm/sec range throughout the sessions (Figure 3A), consistent with other LFP traveling wave studies (Takahashi et al., 2011). The change in traveling wave speeds compared with baseline across time in the session are shown Figure 3B. Note the large increase in slow-delta wave speed after LOC. Alpha and beta waves also significantly increased in speed but much less so than slow-delta waves. After ROC, wave speeds reduced. They remained significantly higher than the awake state but more similar to their prepropofol baseline state.

Changes in the Spatial Structure of Traveling Waves

Propofol also changed the spatial organization of the waves. Specifically, one noticeable change was in their spatial coherence, that is, whether they were more "solid" waves or "broken" waves. A solid wave would show similar amplitudes across adjacent electrodes, and smooth continuous changes across progressively further electrodes. In other words, they had a uniformly organized structure (simulated solid wave Figure 4A, top). A broken wave would, by contrast, show a larger range of amplitude values on the array. As the name suggests, this wave would appear discontinuous on the array (simulated broken wave Figure 4A, bottom). We quantified this using the coefficient of variation (COV: standard deviation divided by the mean) of the amplitude envelope of the traveling wave. Simulated broken waves showed a significantly higher amplitude COV when compared with the more spatially coherent wave (Figure 4B).

We found that slow-delta traveling waves increased their spatial coherence (became more solid) after LOC, whereas alpha and beta waves did the opposite. Figure 4C shows examples of slow-delta waves (moving in the direction of the black arrow) on the vlPFC recording array of Subject 1, in the prepropofol baseline state (top) and after LOC (bottom). The post-LOC slow-delta wave had more amplitude homogeneity than its baseline counterpart, indicating that it was more solid. The change in COV (compared with prepropofol baseline) for slow-delta and beta waves averaged across all arrays, and sessions is shown in Figure 4D. Slow-delta waves showed significantly lower amplitude COV after LOC, indicating more spatial coherence. By contrast, alpha and beta waves became more broken and less structured after LOC, that is, they showed a significant increase in COV relative to the baseline. After ROC, slow-delta waves returned to their baseline coherence. Beta (and to some extent alpha) waves not only regained their structure post-ROC but showed a "rebound." They showed even stronger spatial coherence

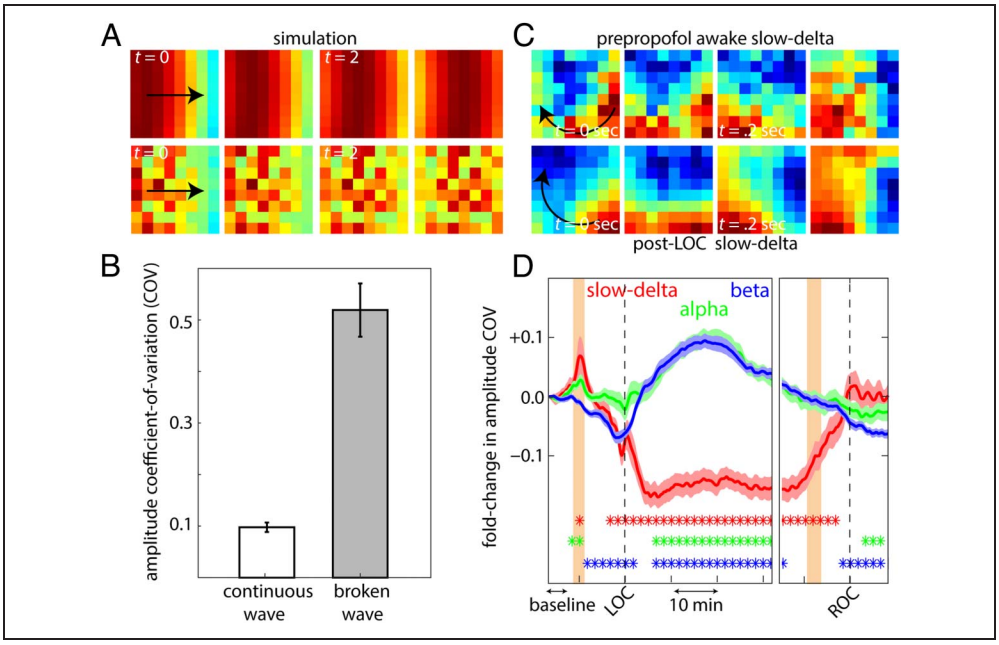

Figure 4. (A) Simulations of traveling waves with different levels of spatial couplings across adjacent elements. Top, solid wave with homogenous amplitude map, and bottom, broken wave with heterogenous amplitude map across the array. (B) Quantification of the COV of amplitudes observed across the array for the simulated solid and broken waves. (C) Example of slow-delta waves observed in the prepropofol state (top) and unconscious state (bottom) for Animal 1. (D) Quantification of the fold change in amplitude COV for slow-delta, alpha, and beta waves compared with baseline (marked) averaged across sessions and arrays. The dots denote statistical significance (blue for beta, green for alpha, and red for slow-delta compared with baseline).

(lower amplitude COV) compared with their prepropofol baseline state.

Propofol Changed Traveling Wave Patterns

In a previous study (Bhattacharya et al., 2022), we demonstrated how one can leverage the properties of three circular–circular correlation coefficients to distinguish between rotating and planar waves (Figure 5A). We applied the same methods here (see Methods section). Both rotating and planar waves were observed in all the recording arrays. On average, during the prepropofol baseline, planar and rotating slow-delta waves had similar incidence on the arrays (Figure 5B).

After LOC, there was a significant decrease in slow-delta rotating waves and increase in slow-delta planar waves (Figure 5B) relative to the slow-delta baseline. This distinction was evident after propofol induction and persisted through LOC. After ROC, slow-delta planar and rotating waves started to converge to their baseline values. By contrast, the changes in alpha and beta wave patterns were more modest. In the alpha-band, planar waves increased and rotating waves decreased. Upon propofol induction, there was a decrease in beta rotating waves and a modest but significant increase in planar waves (Figure 5B). The incidence of beta planar versus rotating waves post LOC was similar to that during baseline. The changes reappeared after propofol cessation

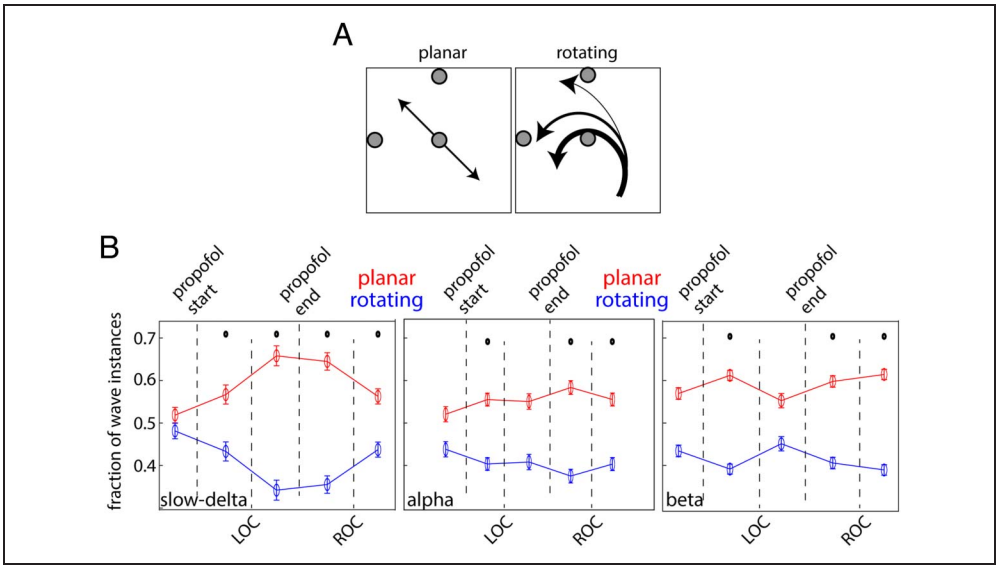

Figure 5. (A) Planar and rotating wave examples, detected with three choice points on the array (gray circles). (B) Fraction of planar and rotating waves noted at different stages of anesthesia for slow-delta (left), alpha (middle), and beta (right) waves averaged across sessions and arrays. Dots denote statistical significance from baseline for each frequency band.

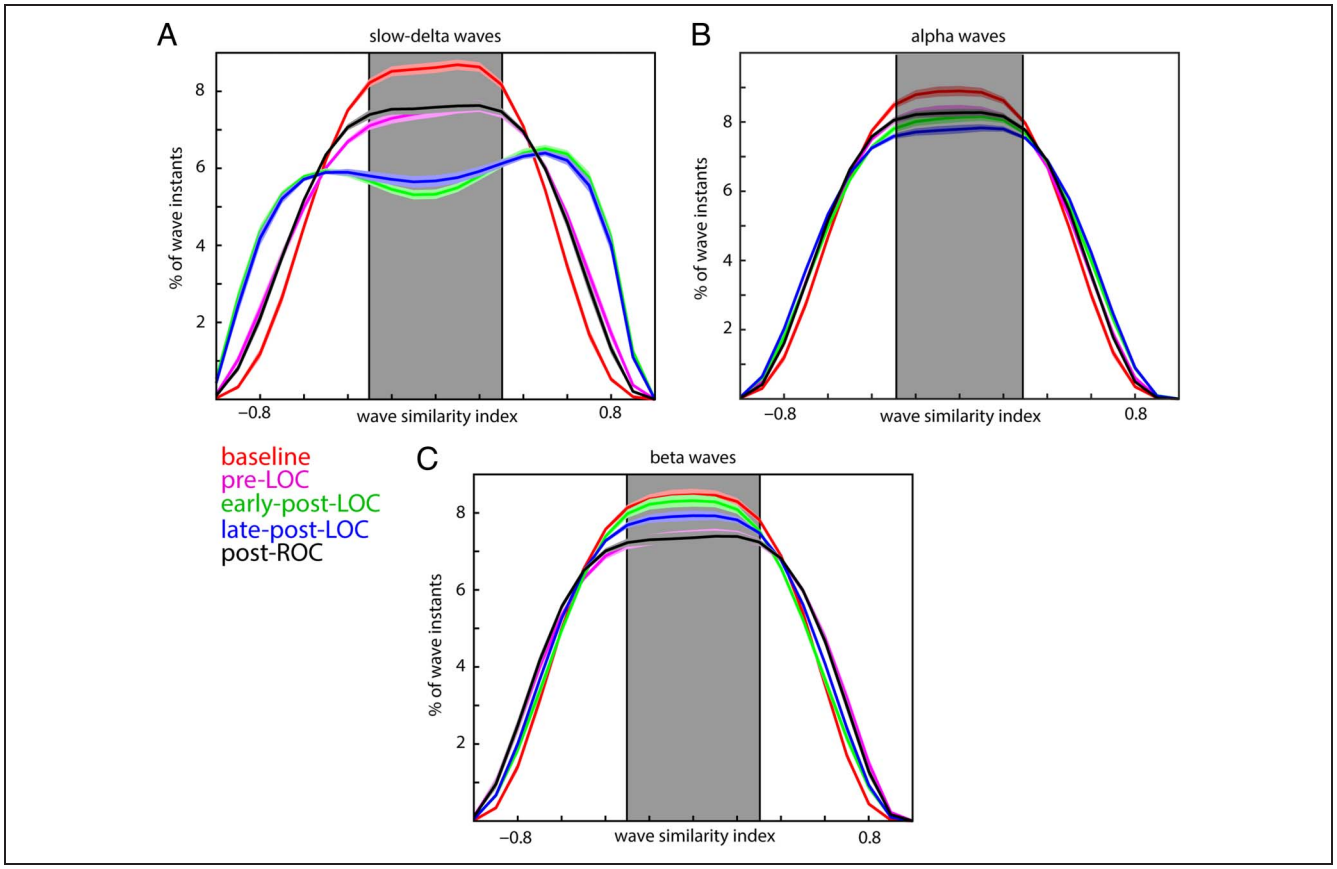

Figure 6. Similarity indices noted for slow-delta (A), alpha (B), and beta (C) waves at different stages of anesthesia, averaged across sessions and arrays. Pre-LOC denotes the period where propofol administration has started but the subject is conscious. Shaded region denotes low similarity values (threshold determined by shuffling permutation procedure; see Methods section).

and in ROC but were modest as well. It is worthwhile to note that the arrays likely captured only part of a larger rotating waves (Bhattacharya et al., 2022). Thus, rotating waves could appear to become more planar if the rotating waves shifted in anatomical location. Nonetheless, these results show that propofol induced changes in wave patterns, especially in the slow-delta band.

Propofol Made Slow-Delta Traveling Waves More Stereotyped

Two waves are similar when they not only have the same direction, but also have similar speed, spatial coherence, and overall organization. They can also be "antisimilar," that is, they are similar in other properties but flow in opposite directions (like a mirror image). We found that after propofol-induced LOC, there was an increase in slow-delta wave antisimilarity.

To quantify this, we performed a similarity analysis on the wave patterns on each array. We calculated, for each array separately, the spatial correlation between each wave at a given snapshot in time with all other waves at other snapshots in time. A positive correlation indicates repetition of a particular wave pattern (i.e., high similarity across time). A negative correlation indicates "antisimilarity," that is, repetition of waves that had high similarity across time but moved in opposite directions. Correlations around zero indicate randomness in wave properties.

Propofol caused an increase in slow-delta wave antisimilarity, relative to baseline. In other words, slow-delta waves became more stereotyped. Figure 6A shows the wave similarity values averaged across arrays and sessions. The distribution for slow-delta traveling waves changed from a more unimodal histogram centered around zero similarity during baseline to a bimodal histogram after LOC. This was verified by fitting a sum of two Gaussian functions with means of opposite signs to the data. The goodness of fit measure improved during unconsciousness (Methods section) suggesting increased bimodality. This meant that slow-delta wave properties were relatively random during baseline but, after LOC, shifted to a repetitive pattern of mirror-image similar waves flowing in opposite directions. This was evident in both early and late periods of unconsciousness (post-LOC; Figure 6A). Then, after ROC, slow-delta waves returned to a unimodal random organization similar to baseline. By contrast, alpha and beta waves (Figure 6B–6C) did not show any shift in the distribution of wave similarity. They were relatively random during baseline and remained so after LOC.

Propofol Caused Slow-Delta and Higher-Frequency Waves to Flow in Mutually Exclusive Directions

Traveling wave directions were also altered after LOC. To quantify this, we classified traveling waves into four different directions. As before, we used two circular–circular correlation coefficients from two choice points in order to capture all wave directions. They were then binned into four directions—toward the four quadrants shown in Figure 7A. The exact wave directions for each recording array depend on the exact placement of the array relative to the waves (Bhattacharya et al., 2022) and preferred direction axes in specific regions (Zhang et al., 2018; Takahashi et al., 2011). Thus, we focus our analyses on the changes in direction after LOC, relative to the awake state.

An example of wave-direction analyses is shown in Figure 7B. It plots the probability of detecting waves in the four binned directions for slow-delta and beta waves during baseline for the vlPFC array of Subject 1 (array location relative to brain sulci is shown on the left). Both slow-delta and beta waves flowed more frequently toward the "red" and "black" zones (see Figure 7A), that is, toward "upper right" and "lower left" of the array. Note that waves from different frequency bands did not necessarily flow in the same directions, as seen here. On other arrays, waves from different frequency bands could have different preferred directions.

Figure 7C shows the change in wave direction on the vlPFC array of Subject 1 post-LOC. Fold change was calculated by dividing the probability of wave detection in each of the four directions with the probability of wave detection in the same direction during baseline. Figure 7C shows this plotted across time averaged across sessions. Slow-delta waves increased toward the directions preferred during baseline (i.e., the red and black directions). By contrast, beta waves reduced in these directions. Instead, they increased toward the green section ("upper left"). Notably, the green direction was least preferred for beta waves during baseline (Figure 7B right). Post-ROC, the wave directions returned to their baseline preferences.

This segregation of slow-delta and beta waves into different directions post-LOC was seen across all arrays. The six arrays were each oriented differently with respect to brain sulci. Plus, the waves were oriented differently with respect to the arrays (Bhattacharya et al., 2022). Thus, we could not simply combine the same directions across arrays (e.g., red to red, black to black). Instead, we rank-ordered the directions based on which directions changed the most from baseline to LOC for beta (black arrow Figure 7C). Rank was assigned based on the signed change. If all directions decreased—Rank 1 would be the direction that decreased the least, whereas Rank 4 would be the direction that decreased the most. If all directions increased, Rank 1 would be the direction that increased the most and so on. That is, the direction that saw the most increase in beta waves after LOC was Rank 1, and the direction that saw the least increase (or most decrease) was Rank 4. We applied the same rank ordering from beta to alpha and slow-delta in order to compare how the directions changed relative to one another. Directions with the same rank were combined across arrays (color coded: red: 1, green: 2, blue: 3, black: 4). We performed the rank-ordering using the beta band because only one direction was enhanced for the beta waves after LOC

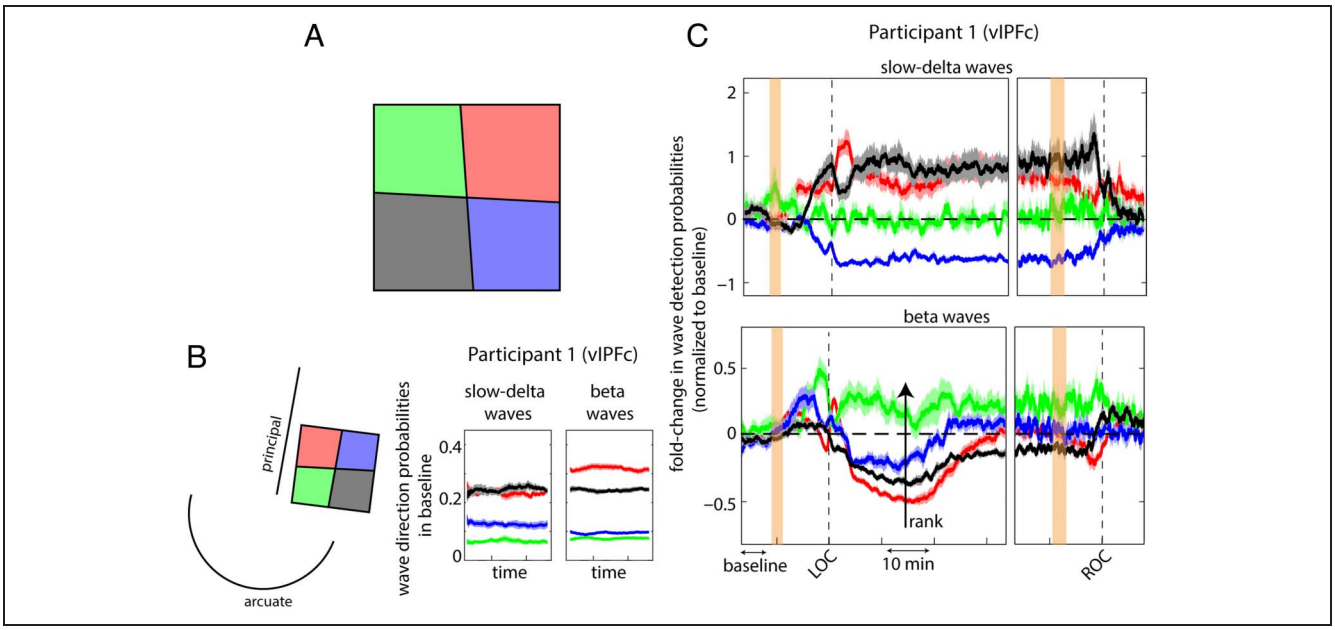

Figure 7. (A) Four direction bins (red, green, blue, and black) along which waves were categorized. (B) Location of vlPFC array of Animal 1 relative to brain sulci (left) and baseline levels of wave direction probabilities (right) for the same array. (C) Fold change in wave detection probabilities in each of the four directions compared with baseline, across time for the same array in B. Black arrow in the beta panel indicates how wave directions were ranked in this particular case (green got Rank 1, whereas red got Rank 4).

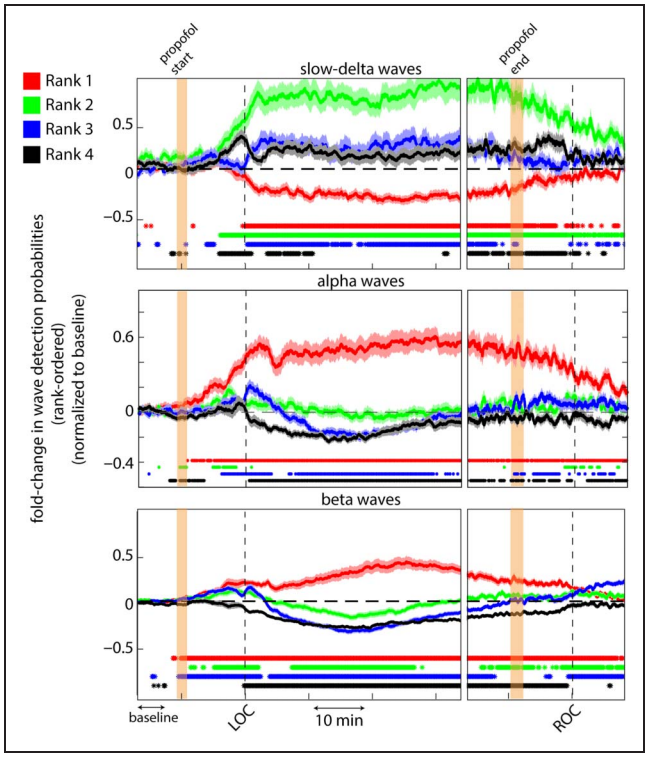

Figure 8. Fold change in wave detection probabilities averaged across all arrays—combined through a rank-ordering system (ranked according to beta wave-change post-LOC as shown in Figure 7). Each color indicates a particular wave direction. Dots denote statistical significance for each direction compared with baseline (t test, $p < .01$).

(slow-delta showed increases in more than one direction). Thus, beta waves provided a straightforward metric to standardize and rank-order changes in direction in other bands.

Figure 8 shows this analysis averaged across all arrays. Post-LOC slow-delta and beta (and alpha) waves increased in mutually exclusive directions. Beta waves increased in one direction (Rank 1, red, by definition) after LOC. By contrast, there was a decrease in beta waves in the other directions (green, blue, and black). Alpha waves behaved similarly as beta waves. Slow-delta waves showed opposite trends to that of beta waves. They increased in the green direction especially but also in the black and blue directions. The red direction, which increased in beta waves, showed a decrease in slow-delta waves. After ROC, wave direction preferences converged (or started to converge) to their prepropofol baseline levels (Figure 8).

DISCUSSION

We found that after propofol-induced LOC, cortical traveling waves were altered. Slow-frequency delta (~1 Hz) waves increased while higher-frequency (8–30 Hz) waves decreased. The slow-delta waves sped up and became more spatially organized. They became more planar (and less rotating) and increased mirror-image waves traveling in opposite directions. Whatever directions slow-delta waves flowed in after LOC, they dominated. Higher-frequency waves decreased and lost structure after LOC, despite showing increased LFP power, and flowed preferentially in directions where slow-delta waves were less frequent.

Our results are in line with previous reports of the effects of propofol and of the properties of traveling waves. The large increase in slow-delta waves after LOC is consistent with prior work showing increases in slow frequency power and coherence in cortex following propofol-induced LOC (Bastos et al., 2021; Redinbaugh et al., 2020, 2021). Our results are also consistent with prior observations that traveling waves (under anesthesia) have preferred directions and mirror-reflective properties (Mitra et al., 2018; Xu, Huang, Takagaki, & Wu, 2007; Sanchez-Vives & McCormick, 2000). They also support a hypothesis by Muller et al. (2018). They posited that decreased spiking activity, as seen under propofol in our earlier work (Bastos et al., 2021), can lead to a greater recruitment of neuron groups into a traveling wave. The result of anesthesia would be more "solid," organized, waves than sparse, "broken" waves. That is what we observed.

Traveling waves under anesthesia seem to cross anatomical boundaries in the visual cortex whereas those in awake state do not (Muller et al., 2014; Xu et al., 2007). This could be explained by our observation of increased slow-delta wave speed and organization after LOC. It could allow waves to travel longer distances without loss of structure (Bhattacharya & Iglesias, 2019). Plus, we observed a decrease in rotating, and an increase in planar, slow-delta waves after LOC. Planar waves can traverse larger distances, as rotating waves tend to lose structure away from their core (Bhattacharya et al., 2022). However, a study in the somatosensory cortex of freely moving mice showed traveling waves spread farther compared with those in mice anesthetized with urethane (Ferezou et al., 2006). The differences between this study and ours could be because of use of a different anesthetic, different species, or a different cortical area (somatosensory cortex). Reimer et al. (2011) reported that traveling waves in rat cortex did not change significantly under different anesthetics (nitrous oxide, isoflurane, or ketamine) but they did not test propofol. We hypothesize that our results may extend to other anesthetics that have similar mechanisms of action through GABAergic circuits (Franks & Lieb, 1994).

The change in slow-delta waves from rotating to planar after LOC could explain differences between sleep and anesthesia. Rotating waves during sleep spindles are associated with memory consolidation by generating spike timing differences that induce spike-time-dependent plasticity (Muller et al., 2016). The "unrotating" of traveling waves by propofol may disrupt those timing relationships and thus potentially explain anesthesia-induced retrograde amnesia.

Unlike slow-delta waves, beta and alpha waves decreased in number and lost structure. It was as if the

slow-delta waves were "swamping" cortex and crowding out the higher-frequency traveling waves and "pushing" them in different directions. Beta and alpha waves did not disappear. They seemed to be redirected by the slow-delta waves. After LOC, higher-frequency (8–30 Hz) waves reoriented to a direction not being used by slow-delta waves. We can perhaps think of wave directions as specific neural pathways/channels. Slow-delta waves after LOC became stronger, more frequent, and more directional—showing a drastic pattern shift from random to mirror-image-like waves. In contrast, higher-frequency waves did not show any pattern shift and deteriorated in structure. We hypothesize that this slow-delta wave dominance caused some pathways to become "crowded" but freed up other pathways to which the higher-frequency waves "retreated," often using channels that were low-preference directions in the awake state.

Beta rhythms are thought to support cognitive functions in NHPs (Bastos, Loonis, Kornblith, Lundqvist, & Miller, 2018; Lundqvist, Herman, Warden, Brincat, & Miller, 2018). Our results indicate that the spatial structure of these rhythms may be important markers of cognition as well. Beta LFP power increased after LOC (albeit less than slow-delta). Beta LFP spatial organization, by contrast, showed different trends. Beta traveling waves decreased, lost structure, and seemed to be forced to change directions by slow-delta waves. Thus, the disruption of traveling waves in the higher frequencies associated with cognition may contribute to LOC under propofol anesthesia.

Acknowledgments

We thank Jesus Ballesteros, Andre Bastos, Alex Major, Dimitris Pinotsis, and Jefferson Roy for helpful comments.

Reprint requests should be sent to Earl K. Miller, The Picower Institute for Learning and Memory, Massachusetts Institute of Technology, 77 Massachusetts Ave, Cambridge, MA 02139, USA, or via e-mail: mekmiller@mit.eduail.

Author Contributions

Sayak Bhattacharya: Formal analysis; Writing—Original draft; Writing—Review & editing. Jacob A. Donoghue: Investigation. Meredith Mahnke: Investigation. Scott L. Brincat: Data curation; Investigation; Methodology. Emery N. Brown: Conceptualization; Supervision; Writing—Review & editing. Earl K. Miller: Conceptualization; Funding acquisition; Project administration; Supervision; Writing—Original draft; Writing—Review & editing.

Funding Information

These studies were supported by ONR MURI N00014-16-1-2832, NIGMS P01GM118269, and The JPB Foundation.

Earl K. Miller, JPB Foundation (https://dx.doi.org/10.13039/100007457), grant number: MIT-PIIF; Office of Naval Research (https://dx.doi.org/10.13039/100000006), grant number: MURI N00014-16-1-2832; National Institute of General Medical Sciences (https://dx.doi.org/10.13039/100000057), grant number: P01GM118269; National Institute of Mental Health (https://dx.doi.org/10.13039/100000025), grant number: R01MH11559.

Diversity in Citation Practices

Retrospective analysis of the citations in every article published in this journal from 2010 to 2021 reveals a persistent pattern of gender imbalance: Although the proportions of authorship teams (categorized by estimated gender identification of first author/last author) publishing in the *Journal of Cognitive Neuroscience* (*JoCN*) during this period were M(an)/M = .407, W(oman)/M = .32, M/W = .115, and W/W = .159, the comparable proportions for the articles that these authorship teams cited were M/M = .549, W/M = .257, M/W = .109, and W/W = .085 (Postle and Fulvio, *JoCN*, 34:1, pp. 1–3). Consequently, *JoCN* encourages all authors to consider gender balance explicitly when selecting which articles to cite and gives them the opportunity to report their article's gender citation balance.

REFERENCES

Alamia, A., & VanRullen, R. (2019). Alpha oscillations and traveling waves: Signatures of predictive coding? *PLoS Biology*, *17*, e3000487. https://doi.org/10.1371/journal.pbio.3000487, PubMed: 31581198

Bastos, A. M., Donoghue, J. A., Brincat, S. L., Mahnke, M., Yanar, J., Correa, J., et al. (2021). Neural effects of propofol-induced unconsciousness and its reversal using thalamic stimulation. *eLife*, *10*, e60824. https://doi.org/10.7554/eLife.60824, PubMed: 33904411

Bastos, A. M., Loonis, R., Kornblith, S., Lundqvist, M., & Miller, E. K. (2018). Laminar recordings in frontal cortex suggest distinct layers for maintenance and control of working memory. *Proceedings of the National Academy of Sciences, U.S.A.*, *115*, 1117–1122. https://doi.org/10.1073/pnas.1710323115, PubMed: 29339471

Benucci, A., Frazor, R. A., & Carandini, M. (2007). Standing waves and traveling waves distinguish two circuits in visual cortex. *Neuron*, *55*, 103–117. https://doi.org/10.1016/j.neuron.2007.06.017, PubMed: 17610820

Bhattacharya, S., Brincat, S. L., Lundqvist, M., & Miller, E. K. (2022). Traveling waves in the prefrontal cortex during working memory. *PLoS Computational Biology*, *18*, e1009827. https://doi.org/10.1371/journal.pcbi.1009827, PubMed: 35089915

Bhattacharya, S., & Iglesias, P. A. (2019). Controlling excitable wave behaviors through the tuning of three parameters. *Biological Cybernetics*, *113*, 61–70. https://doi.org/10.1007/s00422-018-0771-0, PubMed: 30056608

Cowey, A. (1964). Projection of the retina on to striate and prestriate cortex in the squirrel monkey, Saimiri sciureus. *Journal of Neurophysiology*, *27*, 366–393. https://doi.org/10.1152/jn.1964.27.3.366, PubMed: 14168198

Davis, Z. W., Muller, L., Martinez-Trujillo, J., Sejnowski, T., & Reynolds, J. H. (2020). Spontaneous travelling cortical waves gate perception in behaving primates. *Nature*, *587*,

432–436. https://doi.org/10.1038/s41586-020-2802-y, PubMed: 33029013
Ebersole, J. S., & Kaplan, B. J. (1981). Intracortical evoked potentials of cats elicited by punctate visual stimuli in receptive field peripheries. *Brain Research*, *224*, 160–164. https://doi.org/10.1016/0006-8993(81)91126-4, PubMed: 7284831
Ermentrout, G. B., & Kleinfeld, D. (2001). Traveling electrical waves in cortex: Insights from phase dynamics and speculation on a computational role. *Neuron*, *29*, 33–44. https://doi.org/10.1016/s0896-6273(01)00178-7, PubMed: 11182079
Ferezou, I., Bolea, S., & Petersen, C. C. (2006). Visualizing the cortical representation of whisker touch: Voltage-sensitive dye imaging in freely moving mice. *Neuron*, *50*, 617–629. https://doi.org/10.1016/j.neuron.2006.03.043, PubMed: 16701211
Franks, N. P., & Lieb, W. R. (1994). Molecular and cellular mechanisms of general anaesthesia. *Nature*, *367*, 607–614. https://doi.org/10.1038/367607a0
Heitmann, S., & Ermentrout, G. B. (2020). Direction-selective motion discrimination by traveling waves in visual cortex. *PLoS Computational Biology*, *16*, e1008164. https://doi.org/10.1371/journal.pcbi.1008164, PubMed: 32877405
Lewis, L. D., Weiner, V. S., Mukamel, E. A., Donoghue, J. A., Eskandar, E. N., Madsen, J. R., et al. (2012). Rapid fragmentation of neuronal networks at the onset of propofol-induced unconsciousness. *Proceedings of the National Academy of Sciences, U.S.A.*, *109*, E3377–E3386. https://doi.org/10.1073/pnas.1210907109, PubMed: 23129622
Liang, Y., Song, C., Liu, M., Gong, P., Zhou, C., & Knöpfel, T. (2021). Cortex-wide dynamics of intrinsic electrical activities: Propagating waves and their interactions. *Journal of Neuroscience*, *41*, 3665–3678. https://doi.org/10.1523/JNEUROSCI.0623-20.2021, PubMed: 33727333
Lubenov, E. V., & Siapas, A. G. (2009). Hippocampal theta oscillations are travelling waves. *Nature*, *459*, 534–539. https://doi.org/10.1038/nature08010, PubMed: 19489117
Lundqvist, M., Herman, P., Warden, M. R., Brincat, S. L., & Miller, E. K. (2018). Gamma and beta bursts during working memory readout suggest roles in its volitional control. *Nature Communications*, *9*, 394. https://doi.org/10.1038/s41467-017-02791-8, PubMed: 29374153
Massimini, M., Huber, R., Ferrarelli, F., Hill, S., & Tononi, G. (2004). The sleep slow oscillation as a traveling wave. *Journal of Neuroscience*, *24*, 6862–6870. https://doi.org/10.1523/JNEUROSCI.1318-04.2004, PubMed: 15295020
Mitra, A., Kraft, A., Wright, P., Acland, B., Snyder, A. Z., Rosenthal, Z., et al. (2018). Spontaneous infra-slow brain activity has unique spatiotemporal dynamics and laminar structure. *Neuron*, *98*, 297–305. https://doi.org/10.1016/j.neuron.2018.03.015, PubMed: 29606579
Mohan, U. R., Zhang, H., & Jacobs, J. (2022). The direction and timing of theta and alpha traveling waves modulate human memory processing. *bioRxiv*. https://doi.org/10.1101/2022.02.07.479466
Muller, L., Chavane, F., Reynolds, J., & Sejnowski, T. J. (2018). Cortical travelling waves: mechanisms and computational principles. Nature reviews. *Neuroscience*, *19*, 255–268. https://doi.org/10.1038/nrn.2018.20, PubMed: 29563572
Muller, L., & Destexhe, A. (2012). Propagating waves in thalamus, cortex and the thalamocortical system: Experiments and models. *Journal of Physiology, Paris*, *106*, 222–238. https://doi.org/10.1016/j.jphysparis.2012.06.005, PubMed: 22863604
Muller, L., Piantoni, G., Koller, D., Cash, S. S., Halgren, E., & Sejnowski, T. J. (2016). Rotating waves during human sleep spindles organize global patterns of activity that repeat precisely through the night. *eLife*, *5*, e17267. https://doi.org/10.7554/eLife.17267, PubMed: 27855061
Muller, L., Reynaud, A., Chavane, F., & Destexhe, A. (2014). The stimulus-evoked population response in visual cortex of awake monkey is a propagating wave. *Nature Communications*, *5*, 3675. https://doi.org/10.1038/ncomms4675, PubMed: 24770473
Nauhaus, I., Busse, L., Carandini, M., & Ringach, D. L. (2009). Stimulus contrast modulates functional connectivity in visual cortex. *Nature Neuroscience*, *12*, 70–76. https://doi.org/10.1038/nn.2232, PubMed: 19029885
Prechtl, J. C., Cohen, L. B., Pesaran, B., Mitra, P. P., & Kleinfeld, D. (1997). Visual stimuli induce waves of electrical activity in turtle cortex. *Proceedings of the National Academy of Sciences, U.S.A.*, *94*, 7621–7626. https://doi.org/10.1073/pnas.94.14.7621, PubMed: 9207142
Purdon, P. L., Pierce, E. T., Mukamel, E. A., Prerau, M. J., Walsh, J. L., Wong, K. F. K., et al. (2013). Electroencephalogram signatures of loss and recovery of consciousness from propofol. *Proceedings of the National Academy of Sciences, U.S.A.*, *110*, E1142–E1151. https://doi.org/10.1073/pnas.1221180110, PubMed: 23487781
Purdon, P. L., Sampson, A., Pavone, K. J., & Brown, E. N. (2015). Clinical electroencephalography for anesthesiologists: Part I: Background and Basic Signatures. *Anesthesiology*, *123*, 937–960. https://doi.org/10.1097/ALN.0000000000000841, PubMed: 26275092
Redinbaugh, M. J., Afrasiabi, M., Phillips, J. M., Kambi, N. A., Mohanta, S., & Saalmann, Y. B. (2021). Thalamic deep brain stimulation as a paradigm to reduce consciousness: Implications for cortico-striatal dynamics, absence epilepsy and consciousness studies. *bioRxiv*. https://doi.org/10.1101/2021.07.27.453855
Redinbaugh, M. J., Phillips, J. M., Kambi, N. A., Mohanta, S., Andryk, S., Dooley, G. L., et al. (2020). Thalamus modulates consciousness via layer-specific control of cortex. *Neuron*, *106*, 66–75. https://doi.org/10.1016/j.neuron.2020.01.005, PubMed: 32053769
Reimer, A., Hubka, P., Engel, A. K., & Kral, A. (2011). Fast propagating waves within the rodent auditory cortex. *Cerebral Cortex*, *21*, 166–177. https://doi.org/10.1093/cercor/bhq073, PubMed: 20444841
Sanchez-Vives, M. V., & McCormick, D. A. (2000). Cellular and network mechanisms of rhythmic recurrent activity in neocortex. *Nature Neuroscience*, *3*, 1027–1034. https://doi.org/10.1038/79848, PubMed: 11017176
Sato, T. K., Nauhaus, I., & Carandini, M. (2012). Traveling waves in visual cortex. *Neuron*, *75*, 218–229. https://doi.org/10.1016/j.neuron.2012.06.029, PubMed: 22841308
Sreekumar, V., Wittig, J. H., Chapeton, J., Inati, S. K., & Zaghloul, K. A. (2020). Low frequency traveling waves in the human cortex coordinate neural activity across spatial scales. *bioRxiv*. https://doi.org/10.1101/2020.03.04.977173
Takahashi, K., Saleh, M., Penn, R. D., & Hatsopoulos, N. G. (2011). Propagating waves in human motor cortex. *Frontiers in Human Neuroscience*, *5*, 40. https://doi.org/10.3389/fnhum.2011.00040, PubMed: 21629859
Townsend, R. G., & Gong, P. (2018). Detection and analysis of spatiotemporal patterns in brain activity. *PLoS Computational Biology*, *14*, e1006643. https://doi.org/10.1371/journal.pcbi.1006643, PubMed: 30507937
Watt, A. J., Cuntz, H., Mori, M., Nusser, Z., Sjöström, P. J., & Häusser, M. (2009). Traveling waves in developing cerebellar cortex mediated by asymmetrical Purkinje cell connectivity. *Nature Neuroscience*, *12*, 463–473. https://doi.org/10.1038/nn.2285, PubMed: 19287389

Wong, R. O., Meister, M., & Shatz, C. J. (1993). Transient period of correlated bursting activity during development of the mammalian retina. *Neuron*, *11*, 923–938. https://doi.org/10.1016/0896-6273(93)90122-8, PubMed: 8240814

Xu, W., Huang, X., Takagaki, K., & Wu, J. Y. (2007). Compression and reflection of visually evoked cortical waves. *Neuron*, *55*, 119–129. https://doi.org/10.1016/j.neuron.2007.06.016, PubMed: 17610821

Zhang, H., & Jacobs, J. (2015). Traveling theta waves in the human hippocampus. *Journal of Neuroscience*, *35*, 12477–12487. https://doi.org/10.1523/JNEUROSCI.5102-14.2015, PubMed: 26354915

Zhang, H., Watrous, A. J., Patel, A., & Jacobs, J. (2018). Theta and alpha oscillations are traveling waves in the human neocortex. *Neuron*, *98*, 1269–1281. https://doi.org/10.1016/j.neuron.2018.05.019, PubMed: 29887341